The Responses of Antarctic Sea Ice and Overturning Cells to Meridional Wind Forcing

HAJOON SONG,[a,b] YEONJU CHOI,[a] EDWARD W. DODDRIDGE,[c] AND JOHN MARSHALL[d]

[a] *Department of Atmospheric Sciences, Yonsei University, Seoul, South Korea*
[b] *Division of Environmental Science and Engineering, Pohang University of Science and Technology, Pohang, South Korea*
[c] *Australian Antarctic Program Partnership, Institute for Marine and Antarctic Studies,
University of Tasmania, Hobart, Tasmania, Australia*
[d] *Department of Earth, Atmospheric and Planetary Sciences, Massachusetts Institute of Technology, Cambridge, Massachusetts*

ABSTRACT: Meridional winds over the seasonal ice zone of the Antarctic have undergone changes and likely contributed to sea ice extent variability in recent decades. In this study, using observations and an eddy-resolving channel model of the Antarctic seasonal ice zone, we investigate the influence of meridional wind changes on the sea ice distribution and document how the underlying ocean might change. We find that southerly wind anomalies in austral winter lead to an increase in sea ice extent by encouraging equatorward sea ice drift. This results in more leads and polynyas, ice production, and buoyancy loss near the coastal region and freshening out in the open ocean near the Antarctic Circumpolar Current. In contrast, summertime southerly wind anomalies reduce sea ice extent due to warming anomalies near the sea ice edge. This is a consequence of enhanced meridional overturning circulation (MOC) triggered by enhanced buoyancy loss through surface heat flux and brine rejection, which brings relatively warm water toward the summertime sea ice edge. A water-mass transformation analysis reveals the increased bottom water formation caused by brine rejection and heat loss in leads and polynyas. Changes in sea ice extent and MOC behave in the opposite way when the sign of the wind anomaly is switched from southerly to northerly. Our study shows that meridional wind anomalies can modify not only the sea ice distribution, extent of polynyas, and air–sea buoyancy fluxes but also the ocean's MOC and bottom water properties.

KEYWORDS: Sea ice; Southern Ocean; Meridional overturning circulation; Idealized models; Ocean models

1. Introduction

Antarctic sea ice is a crucial element in the complex interplay between the atmosphere and the ocean. While sea ice typically impedes the exchange of heat and gases between the ocean and atmosphere, certain areas known as leads and polynyas allow for intense heat loss to occur (Smith et al. 1990; Morales Maqueda et al. 2004; Campbell et al. 2019). This heat loss can trigger the formation of new sea ice and the subsequent salt flux into the ocean through brine rejection (Tamura et al. 2008). These processes are critical for the ventilation of the ocean and the formation of bottom water, highlighting the importance of Antarctic sea ice in the global climate system (Ferrari et al. 2014). Additionally, the regulation of heat and moisture fluxes by sea ice, together with its effect on albedo and thence radiation streams, impacts atmospheric inversions (Pavelsky et al. 2011), low-level cloud formation (Wall et al. 2017), and the tropospheric jet (Smith et al. 2017; Bader et al. 2013; Kidston et al. 2011) by modulating near-surface temperature and humidity. For example, sea ice suppression of oceanic heat transfer typically strengthens atmospheric inversions, an effect which decreases at higher altitudes (Pavelsky et al. 2011). These stratification changes affect baroclinic instability, altering the tropospheric jet's strength and location (Smith et al. 2017). Moreover, Antarctic sea ice plays a crucial role in the global climate system by influencing the carbon cycle through the modulation of air–sea carbon exchange and the vertical mixing of the ocean (Stein et al. 2020).

Satellite observations show that the extent of Antarctic sea ice generally increased from the beginning of the record in the late 1970s until 2014, albeit with spatial and temporal variability (Simmonds and Li 2021; Turner et al. 2016; Comiso et al. 2017; Parkinson and Cavalieri 2012; Cavalieri and Parkinson 2008; Comiso and Nishio 2008). This multidecadal increase in Antarctic sea ice contrasts with the decrease in Arctic sea ice caused by global warming (Simmonds and Li 2021; Turner et al. 2009). It should also be noted, however, that in the last decade or so, Antarctic sea ice extent (SIE) has also shown marked downward excursions but with significant interannual variability (Purich and Doddridge 2023; Simmonds and Li 2021). The counterintuitive behavior of Antarctic sea ice in a generally warming world has led to extensive related studies on causes and mechanisms, such as changes in westerly winds (Purich et al. 2016; Thompson and Solomon 2002; Ferreira et al. 2015), ocean currents and upwelling (Armour et al. 2016), and freshwater input from ice sheets (Pauling et al. 2016; Bintanja et al. 2013; Rye et al. 2020).

In the Antarctic region, changes in sea ice extent are also associated with changes in the meridional wind (Holland and Kwok 2012; Haumann et al. 2014, 2016; Turner et al. 2016; Kwok et al. 2017). Holland and Kwok (2012) show that changes in local wind can account for the trend in sea ice drift and concentration in West Antarctica. Haumann et al. (2014) and Turner et al. (2016) also suggest that changes in wind patterns associated with surface pressure systems are linked to changes in Antarctic sea ice on multidecadal time scales, although they differ in their explanation for these changes; Haumann et al. (2014) attribute it to anthropogenic stratospheric ozone depletion

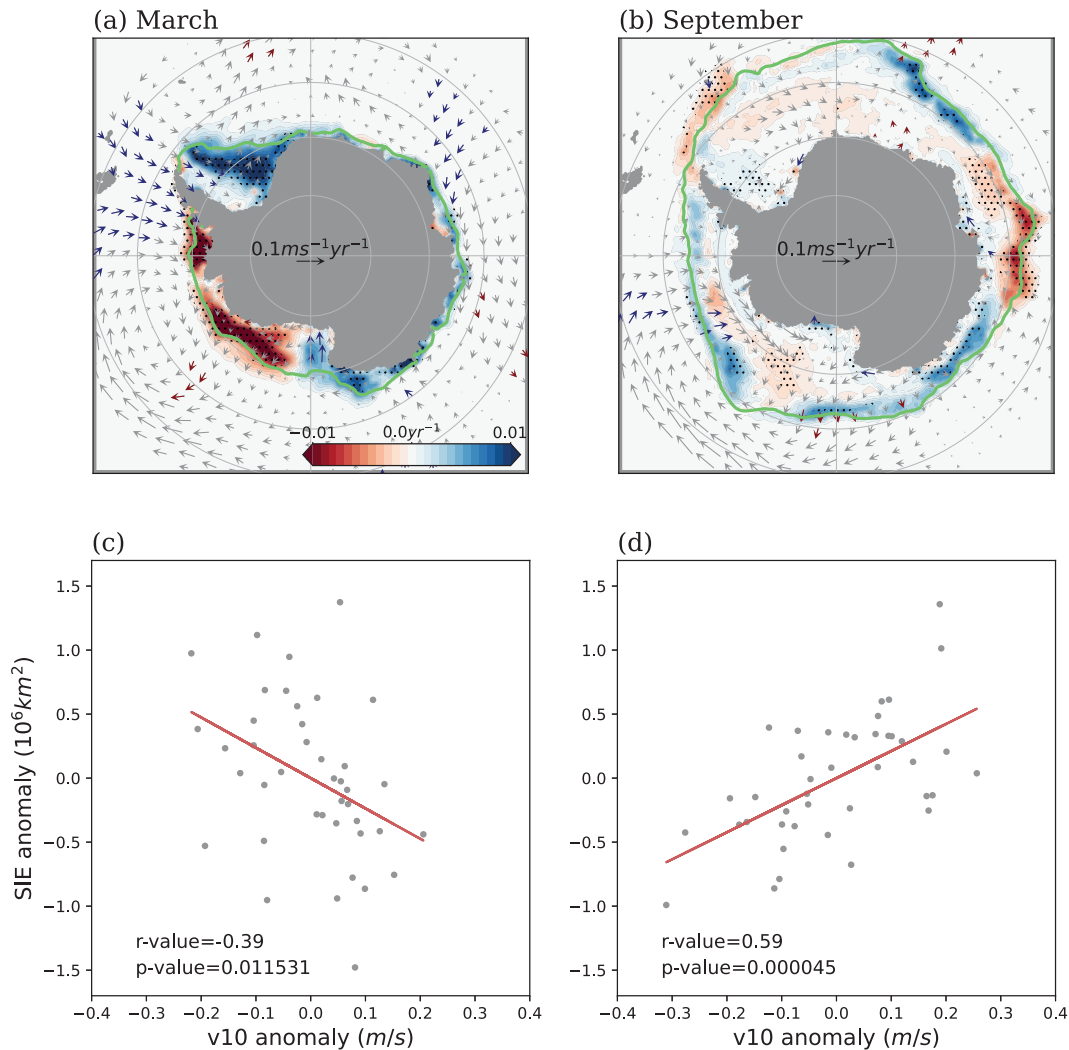*Corresponding author*: Hajoon Song, hajsong@yonsei.ac.kr

FIG. 1. (a),(b) The trend of SIC (shades) and 10-m wind (arrows) and (c),(d) the relationships between the anomalies of SIE and 10-m meridional wind (v10) for (a),(c) March and (b),(d) September during 1980–2020. In (a) and (b), stippling indicates SIC trends with >95% significance, while red and blue vectors, respectively, signify positive and negative equatorward meridional wind trends with >90% significance, respectively. Green lines in (a) and (b) denote the average sea ice edge determined by the location where the seasonal sea ice concentration, averaged from 1980 to 2020, is at 15%. Data sources: NSIDC satellite product (SIC) and ERA5 reanalysis data (10-m wind).

and greenhouse gas increase, while Turner et al. (2016) suggest that the intensified southerly winds fall within the intrinsic variability of the climate system. Haumann et al. (2016) find the intensifying trend of the southerly wind is responsible for the recent increase in northward sea ice extent and freshwater transport. Notably, the sea ice extent and the southerly wind show seasonally varying correlation (Fig. 1). There are perhaps two-way interactions between the meridional wind and sea ice extent and indeed Kwok et al. (2017) attribute the seasonal trends in meridional winds to that of Antarctic sea ice extent.

The observed significant correlation between meridional wind anomalies and Antarctic sea ice trends is not fully understood due to the influences of multiple other factors. In particular, the zonal component of the wind over the Antarctic sea ice is generally stronger than the meridional component (Hazel and Stewart 2019). The strong easterlies around Antarctica make it challenging to isolate the individual effects of meridional wind anomalies on regional sea ice trends. Moreover, they are intimately connected through dynamics. Southerly katabatic winds, which are not typically included in numerical models, are deflected to the left by the Coriolis force thus inducing an easterly component (Parish and Waight 1987). Finally, the large spread in meridional wind trends across various reanalysis products adds a note to caution due to the high level of uncertainty in estimating such changes (Dong et al. 2020; Neme et al. 2022).

Coastal polynyas are also sensitive to southerly winds blowing off the Antarctic landmass (Dale et al. 2017; Pease 1987).

These polynyas are key contributors to the formation of dense, saline waters on the shelf which cascade down the continental slope to form Antarctic Bottom Waters (AABWs). Open ocean convection can also contribute to AABW but, as reviewed in Silvano et al. (2023), the shelf is thought to be the primary source. Thus, katabatic winds play an important role, particularly in driving the deep circulation of the Southern Ocean.

In this study, we employ a high-resolution three-dimensional channel model to investigate the response of Antarctic sea ice and Southern Ocean circulation to changes in meridional winds. The idealized model allows us to focus on dynamical connections between the meridional wind perturbation and the Southern Ocean states, including sea ice and overturning circulation, by eliminating complexities that might arise from factors such as bathymetry and surface forcing. Our idealized model captures the seasonal cycle of sea ice together with key ocean circulation features, including the Antarctic Circumpolar Current, Antarctic Slope Current, the two-cell structure in the meridional overturning circulation, and in particular its deep cell associated with AABW (Doddridge et al. 2021). Our goals are to 1) examine the effects of meridional wind anomalies on sea ice concentration and its seasonal cycle; 2) explore how changes in sea ice concentration affect water-mass transformation in the Southern Ocean; 3) investigate the impact of meridional wind anomalies on ocean circulation; and 4) identify key mechanisms and feedbacks at play in goals 1), 2), and 3). We find that meridional wind changes over Antarctic sea ice can indeed trigger substantial changes in the cycle of sea ice, extent of polynyas, the ocean state, and the strength of the lower cell.

Our paper is organized as follows. In section 2, we analyze satellite observations and reanalysis to identify the relationship between meridional winds and the cycle of Antarctic sea ice. We then describe our model, experimental design, and analysis methods in section 3. The response of sea ice and ocean states to the meridional wind anomalies is presented in section 4, while section 5 examines changes in ocean circulation and associated water-mass transformation rates. Finally, we summarize and discuss implications in section 6.

2. Observational analysis of meridional winds and sea ice extent

We analyze the relationship between meridional wind and Antarctic sea ice, focusing on sea ice concentration and 10-m wind trends in March (minimum sea ice extent) and September (maximum extent) from 1980 to 2020 (Fig. 1). We obtained the monthly mean sea ice concentration data from the NASA National Snow and Ice Data Center (DiGirolamo et al. 2022) and the 10-m wind data from the fifth major global reanalysis produced by European Centre for Medium-Range Weather Forecasts (ECMWF) (ERA5) (Hersbach et al. 2023).

In summer, there is a trend of deepening of the Amundsen Sea low (ASL), a low pressure system observed in the mean sea level pressure near the Amundsen Sea, while the opposite trend occurs over the Weddell Sea and Indian Ocean (Fig. 1a). The strengthening of both cyclone and anticyclone within the western Antarctic Ocean accompanies strong northerly wind

trends over the Antarctic Peninsula and southerly wind trends over the Ross Sea and the northeastern Weddell Sea near 10°–20°W. Meanwhile, in winter during this period, only the strengthening tendency of ASL is significant with its center shifted southwestward (Fig. 1b). The contrast in sea ice concentration trends between the western and eastern regions of the Antarctic Peninsula may be related to changes in the ASL and associated meridional wind variability.

Scatterplots in Figs. 1c and 1d illustrate the relationship between anomalies of meridional wind and sea ice extent, the total area of grid cells with sea ice concentration exceeding 15%. The positive correlation between them during the austral winter suggests that the anomalously strong southerly wind tends to extend the sea ice edge equatorward in winter (Fig. 1d). This positive correlation is consistent with the results of several previous studies (Wagner et al. 2021; Turner et al. 2016; Stammerjohn et al. 2003; Holland and Kwok 2012). Austral summer, on the other hand, shows a negative relationship between meridional wind anomaly and sea ice extent anomaly. Although this correlation is weaker and less significant than in winter, it is still significant ($p = 0.011531$) (Fig. 1c). This weak correlation suggests that thermodynamic processes, driven by local radiative equilibrium or thermal advection within both the ocean and atmosphere, may play a bigger role in sea ice variability during summer months than dynamic redistribution by wind stress. Alternatively, it is difficult to dismiss the possibility that the strong correlation observed in winter could influence summer sea ice minimum. Historically, there has been little relationship between the winter states and subsequent summer minimum (Libera et al. 2022), and it may differ on larger time scales or due to rapid shifts in the Antarctic sea ice system.

Furthermore, uncertainties in the satellite sea ice data increase during summer months, as distinguishing melt ponds from open water and capturing rapid melting events become challenging. These results suggest the necessity for further analyses of how sea ice responds differently to meridional wind anomalies in summer and winter and how these changes are related to ocean circulation. It could provide useful insights to investigate the underlying mechanisms that drive these observed correlations using a numerical model.

3. Experiments with an eddying channel model of the seasonal ice zone

a. Channel model

A channel model is prepared using MIT General Circulation Model (MITgcm) (Marshall et al. 1997a,b; Adcroft et al. 1997; Marshall et al. 1998; Adcroft et al. 2004) to represent the sea ice and ocean circulation in the Southern Ocean. The domain has a size of 1200 km × 3200 km in zonal and meridional directions, respectively, with 4-km resolution. Considering that the first baroclinic Rossby radius of deformation is approximately 10 km near 60°S (Chelton et al. 1998), the mesoscale eddies are resolved in most of the model domain. There are 50 vertical levels from the surface to 4000 m. The upper 50 m is resolved at every 10 m, and the intervals
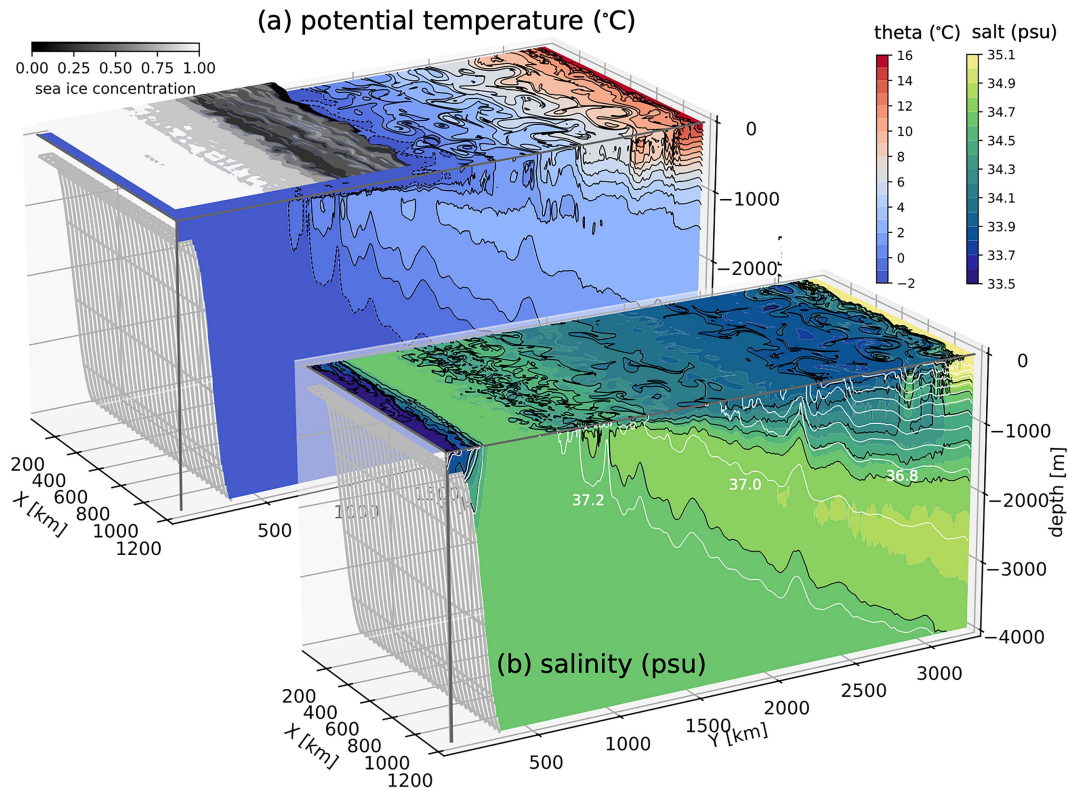
(a) potential temperature (°C)

FIG. 2. An instantaneous plot from Austral winter (1 September) of our re-entrant channel solution showing (a) potential temperature (shading and black contours) with sea ice fraction overlaid and (b) salinity (shading and black contours) and σ_2 (the potential density referenced to 2000 dbar, white contours with interval 0.2 kg m^{-3}).

between levels increase to 100 m toward the bottom. This configuration has a flat bottom, but there is a 300-m-deep, 80-km-wide shelf near the southern boundary that drops to the bottom within 300 km (Fig. 2). The model has connected east and west boundaries, allowing the flow to leave from one end and re-enter from the other, while the northern and southern boundaries are closed.

The temperature and salinity data from the *World Ocean Atlas*, version 2 (Locarnini et al. 2013; Zweng et al. 2013), along I6 near 30°E were used to initialize the model domain. This meridional section has relatively simple bathymetry and clear hydrographic characteristics which are typical of the Southern Ocean, such as a temperature inversion. The data were extended zonally to cover the entire domain. The northern boundary has an approximately 100-km-wide sponge layer where temperature and salinity are restored to the climatology with a time scale that changes from infinity at the southern edge to 10 days at the northern edge of the sponge. In addition, we simulate the dynamics and thermodynamics of sea ice by initializing the sea ice model with a 1-m-thick ice cover south of 56°S. The simulation does not include an active ice shelf processes, which can lead to missing key processes such as ice shelf basal melt that are crucial for bottom water formation.

The ocean in the channel was forced by the monthly mean atmospheric data from the Corrected Normal Year Forcing,

version 2.0, product (Large and Yeager 2009) through bulk formulae (Large and Pond 1982). Similar to the initial condition, the values along 30°E were extended to cover the channel, so there is no variation in surface forcing in the zonal direction. The vertical Laplacian viscosity is set to 1.0×10^{-3} m^2 s^{-1}, and vertical mixing for the tracers is computed by the turbulent kinetic energy scheme by Gaspar et al. (1990) with the background value of 1.0×10^{-5} m^2 s^{-1}. Additionally, implicit vertical diffusivity for convection is set to 10 m^2 s^{-1} for convective mixing due to static instabilities. The model was then integrated for 50 years to reach the quasi-equilibrium state. The runoff from the Antarctic continent, which can influence the ocean states and circulation (Purich and England 2023), is not represented in this model. The detailed configuration can be obtained online (https://doi.org/10.5281/zenodo.11195066).

b. Meridional wind perturbation

We investigate the impact of meridional wind on the state of sea ice and the ocean, as well as water-mass transformation, by adding a perturbation to the meridional wind field south of 59°S. The size of the wind perturbation, v'_{10m}, is defined as a function of latitude ϕ following

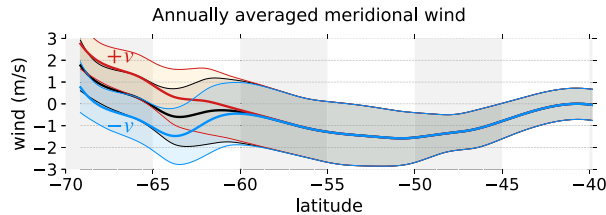$$v'_{10m}(\phi) = \frac{1}{\exp[(\phi - \phi_0)/\lambda] + 1}. \tag{1}$$

FIG. 3. Zonally averaged 10-m meridional wind applied to the channel model, along with its positive and negative perturbations. The solid black, red, and blue lines represent the annually averaged meridional wind in CTRL, $+v$, and $-v$, respectively, with the shading representing their standard deviation. The wind in CTRL is from CORE forcing.

With $\phi_0 = 62°S$ and $\lambda = (10/12)°$, the wind perturbation becomes 0.5 m s^{-1} at $\phi = 62°S$ and approaches 1 and 0 m s^{-1} toward the pole and equator, respectively, within a few degrees of latitude (Fig. 3). This perturbation is applied to the monthly averaged meridional wind for the entire year. We refer to the simulation with this perturbation added to the meridional wind as $+v$ and to the simulation with this perturbation subtracted from the meridional wind as $-v$. The perturbation of 1 m s^{-1} is one order of magnitude smaller than the meridional wind correction used in previous studies (Kim and Stössel 1998; Barthélemy et al. 2012) and is of similar magnitude to the standard deviation of the meridional wind (as shown in shading in Fig. 3). Moreover, the changes of the meridional wind over 10 years are on the order of 0.1 m s^{-1} yr^{-1} (Holland and Kwok 2012), which all suggest that the size of perturbation used in this study is reasonable. With the initial condition taken from the 50-yr of spinup simulation, we integrate the channel model with this wind perturbation for an additional 16 years and analyze the last 10 years by comparing the results with the control simulation (CTRL) where there is no meridional wind perturbation.

c. Analysis in density coordinates: Residual overturning circulation and water-mass transformation rate

We evaluate the impact of meridional wind perturbations on the oceanic overturning circulation. The residual overturning circulation is the result of a balance between the wind-driven circulation and the circulation associated with eddies and can be directly obtained using the transport weighted by the thickness of a given layer (Marshall and Speer 2012; Pinardi et al. 2019). It is computed at every model time step using the LAYERS package in MITgcm (Abernathey et al. 2016). For this calculation, we define 122 classes of σ_2 (potential density referenced to 2000 dbar) covering from 33.5 to 37.8 kg m^{-3} with nonuniform spacing. The interval is as little as 0.01 kg m^{-3} from 37.4 to 37.8 kg m^{-3} and larger elsewhere.

The residual overturning circulation can be further analyzed by examining the water-mass transformation rate. The changes in volume between isopycnal surfaces are primarily driven by the divergence of the advective volume flux along isopycnals and the volume flux across the isopycnal surfaces. The latter requires buoyancy fluxes, which change the density

of water, and occurs either through surface buoyancy fluxes or diapycnal mixing across isopycnals. Our interest is on the contribution of surface buoyancy fluxes to the volume flux across isopycnal surfaces, which is also known as the water-mass transformation rate, and its relationship with the residual overturning circulation.

A volume of fluid of uniform density changes when there is a flow $\mathbf{v}$ through the isopycnals that confine this volume or when the interface of isopycnal moves with $\mathbf{v}_\sigma$, an isopycnal velocity, without actual volume flux. Then, the diapycnal volume flux $A(\sigma, t)$ can be expressed as

$$A(\sigma, t) = \iint_{\mathscr{A}_\sigma(\sigma,t)} (\mathbf{v} - \mathbf{v}_\sigma) \cdot \hat{\mathbf{n}}_\sigma d\mathscr{A}, \qquad (2)$$

where $\mathscr{A}_\sigma(\sigma, t)$ is the area of isopycnal surface and $\hat{\mathbf{n}}_\sigma$ is a unit vector normal to the isopycnal surface pointing from low to high values. The diapycnal volume flux is further shown to be related to the nonadvective supply of buoyancy (Walin 1982; Marshall et al. 1999; Nishikawa et al. 2013; Al-Shehhi et al. 2021), which can be written as

$$A = F - \frac{\partial D}{\partial \sigma}, \qquad (3)$$

where F is associated with surface fluxes and the second term is associated with diffusive fluxes within the ocean. The F, known as "transformation rate," can be written using the heat flux $\mathcal{Q}_{net}$ and freshwater flux $\mathscr{F}_{FW}$ so that

$$F = \frac{\partial}{\partial \sigma} \iint_{\mathscr{A}_s(\sigma,t)} \left(\frac{\alpha}{c_w} \mathcal{Q}_{net} + \rho_0 \beta S \mathscr{F}_{FW} \right) d\mathscr{A}. \qquad (4)$$

Here, ρ_0 is the reference density, α is the thermal expansion coefficient for seawater, c_w is the heat capacity of water, β is the haline contraction coefficient, and S is the local surface salinity. Both $\mathcal{Q}_{net}$ and $\mathscr{F}_{FW}$ are positive when they increase the surface density.

4. Response of sea ice and ocean states to meridional wind perturbations

a. Sea ice responses

The idealized channel model simulates the mean states of Antarctic sea ice and its seasonal variation with reasonable accuracy. Although the simulated sea ice extent has smaller seasonality and rather slow melting, the total sea ice extent in both summer and winter in CTRL is comparable with observations [Ocean and Sea Ice Satellite Application Facility (OSI SAF) 2022], despite its simple bathymetry and zonally symmetric surface forcing (not shown). Additionally, the annual sea ice production is approximately 900 ± 22 km^3 when estimated using the sea ice fraction, the mean thickness, and the area of each model grid. This is equivalent to approximately 13 950 km^3 if we linearly extend the production to the zonal length of the Southern Ocean, which is remarkably close to an observational estimate of 13 000 km^3 based on satellite observations (Tamura et al. 2008).

The seasonality of sea ice extent is modified by the meridional wind perturbation. The $+v$ run produces a greater sea ice extent in winter but lower in summer compared to CTRL, whereas the $-v$ run shows the opposite pattern, with slightly lower sea ice extent in winter but greater in spring (Fig. 4a). Interestingly, changes in sea ice volume differ from those in sea ice extent (Fig. 4b). The $-v$ run shows the greatest sea ice volume throughout the year with the least seasonality. In $-v$, much of the sea ice is under the northerly wind (Fig. 3), which prevents the sea ice from drifting equatorward away from its formation site. As a result, the sea ice can grow more in $-v$ and becomes approximately 13% thicker than CTRL on average. In March, the sea ice thickness in $-v$ is nearly 30% greater than CTRL. On the other hand, the $+v$ run exhibits the largest seasonal variability of sea ice volume, indicating maximum sea ice production. In the final year of the simulation, sea ice production in $+v$ exceeded 1×10^3 km^3, nearly 70% greater than in $-v$. The greater seasonality in $+v$ suggests a more active equatorward freshwater transport by sea ice, leading to lower salinity with the melting of the sea ice following winter.

The impact of the meridional wind on the sea ice horizontal distribution is clearly evident from Figs. 4c–e, which displays the sea ice concentration in July of the last simulation year when the sea ice extends at least 58°S in all simulations. The visual comparison shows that the $-v$ run has the highest concentration between 65° and 61°S, but the lowest concentration to the north of 61°S (Fig. 4c). In contrast, the $+v$ run exhibits the greatest sea ice concentration to the north of 61°S, but lower than the $-v$ run between 65° and 61°S (Fig. 4e). In addition, there are polynyas near 65°S in $+v$ where the ocean loses massive quantities of heat (nearly 300 W m^{-2}) to the atmosphere (indicated by red dots in Fig. 4e). These polynyas, resulting from the divergence of sea ice driven by southerly wind, are also the site of sea ice production, leading to density increase through brine rejection.

To the south of 65°S, $+v$ has the areas with the salt flux greater than 5×10^{-4} psu kg m^{-2} s^{-1} (green dots in Fig. 4e). These regions are largely ice covered (sea ice concentrations of greater than 80%) but have lower sea ice concentration than their surroundings with values close to 1 indicating complete sea ice coverage of the grid cell that may be associated with leads. Despite the sea ice concentration being greater than 0.8 in these areas, there is a continuous release of salt to the ocean due to ongoing sea ice production. The brine rejection associated with sea ice production shows up as regions of large salt fluxes. The forthcoming water-mass formation analysis in section 5b will further emphasize the importance of these regions for the circulation of the Southern Ocean.

We now analyze the sea ice changes in $+v$ and $-v$ using the sea ice volume (Φ) flux and its budget. Equatorward sea ice export is significantly larger during the ice growth season (from March to September) than the melt season (from September to March) (Figs. 5a,b). The maximum sea ice export occurs at 65°S (Fig. 5b), mainly as a result of large sea ice volume. The sea ice's movement is suppressed in the areas with higher ice concentration and thickness, where internal ice stress is strong at latitudes higher than 65°S, as suggested

by the high sea ice concentration (SIC) values in Fig. 6b. Another peak in sea ice export is observed near 59° to 60°S, driven by strong westerly winds causing a significant northward (or equatorward) sea ice drift when sea ice expands to this westerly band in late autumn. During the melt season, sea ice export significantly decreases (Fig. 5a), with certain summer months even experiencing poleward export (not shown), likely due to northerly winds.

The meridional wind perturbation significantly alters the amount of sea ice export. In the $+v$ run, equatorward export increases throughout the sea ice zone, exhibiting a substantial export even near the coast at 69°S where there is nearly negligible export in the CTRL and $-v$ runs. This difference is due to stronger southerly winds in the $+v$. In contrast, the southerly wind in the $-v$ run is close to zero and sometimes reverses to become a northerly wind which compresses sea ice toward the coast. The pronounced ice export from the coastal region in the $+v$ run implies an increased production of sea ice near the coast in the $+v$ run, as anticipated in Fig. 4.

The analysis of the sea ice volume budget using zonally averaged monthly mean model outputs, as illustrated in Figs. 5c–h), underscores the role of meridional wind-induced changes in sea ice production and distribution. The equation governing the evolution of zonal-averaged ice volume, Φ, is

$$\frac{\partial \Phi}{\partial t} = -\frac{\partial (v_{\text{ice}} \Phi)}{\partial y} + \Gamma_\Phi. \tag{5}$$

The right-hand side depicts the two major contributors to the ice volume change. The first term represents the meridional transport of sea ice volume, where v_{ice} denotes the meridional ice drift velocity. The meridional transport term $v_{\text{ice}} \Phi$ is calculated online during simulations. The second term Γ_Φ represents the thermodynamic processes, like freezing and melting, and is determined offline as the residuals from the total monthly volume change minus the convergence of the transport. This budget analysis shows the latitudes where wind changes lead to additional sea ice freezing or melting and further illustrates the balance between thermodynamic sources and dynamic redistribution in both season and latitude.

During the melt season, the time derivative of sea ice concentration is primarily governed by the thermodynamic sink (melting, Figs. 5c,g) rather than the dynamic term (convergence of sea ice volume flux, Fig. 5e). In the growth season, equatorward of 65°S, dynamic redistribution generally makes a larger contribution to the sea ice volume changes, except near 61°S, and determines the position of the sea ice edge. Freezing and divergence largely counterbalance each other to the south of 65°S (Figs. 5d,f,h), which suggests an active manufacturing and equatorward transport of the sea ice there. This is particularly evident at the peaks at 66°–67° and 65°S, areas characterized by leads and polynyas (Fig. 4d). This is consistent with the balance between dynamic/thermodynamic tendencies found by Schroeter and Sandery (2022).

The meridional wind perturbations clearly alter sea ice production and distribution (Figs. 5c–h). In the $+v$ run, the rate of sea ice volume change is larger than other simulations in both the growth and melt seasons (Figs. 5c,d). Furthermore,
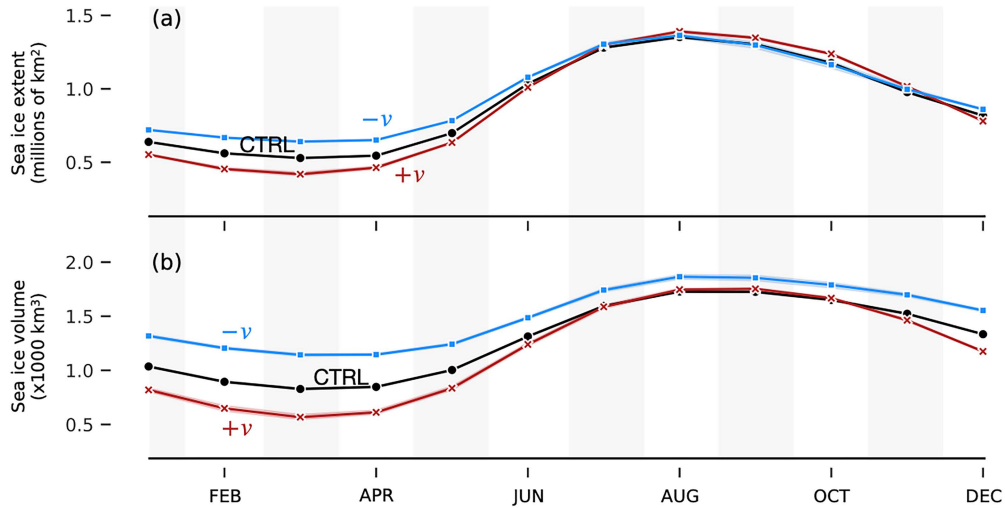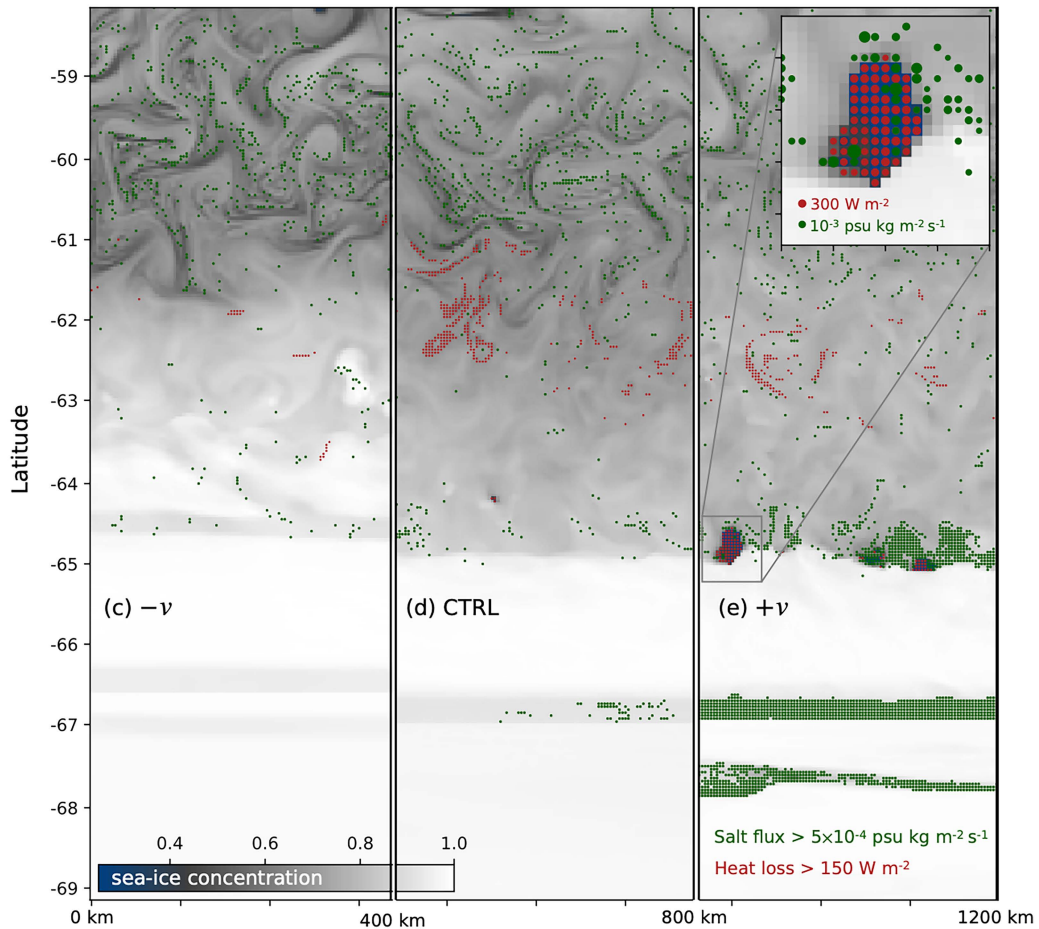
FIG. 4. Monthly mean annual cycle of (a) sea ice area and (b) sea ice volume from CTRL (black line), $+v$ (red line), and $-v$ (blue line) averaged over 10 years. The subtle shading indicates one standard deviation. A July instantaneous sea ice concentration is shown in (c) for the $-v$ wind perturbation, (d) CTRL (no wind perturbation), and (e) for the $+v$ perturbation. Red and green dots in (c)–(e) represent those points where the ocean heat loss to the atmosphere exceeds 150 W m^{-2} and the salt flux exceeds 5×10^{-4} psu kg m^{-2} s^{-1}, respectively. The size of the red and green dots in the inset in (e) is scaled with reference to 300 W m^{-2} and 1×10^{-3} psu kg m^{-2} s^{-1}, respectively.
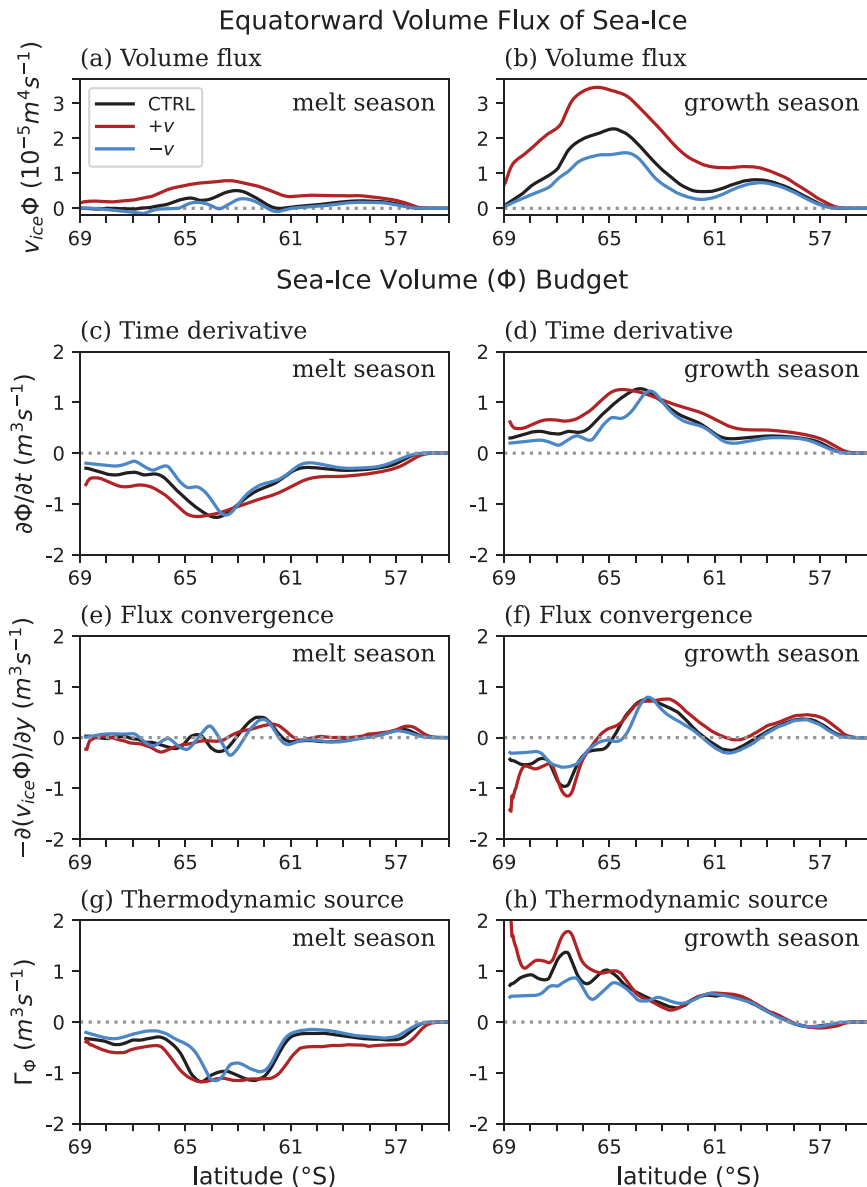
Equatorward Volume Flux of Sea-Ice

FIG. 5. (a),(b) Equatorward flux of sea ice volume (Φ) and (c)–(h) the sea ice volume budgets from CTRL, $+v$, and $-v$ wind perturbations. (left) The melt season (September–March) and (right) the growth season (March–September). The sea ice volume budgets include (c),(d) the time derivative ($\partial\Phi/\partial t$), (e),(f) flux convergence [$-\partial(v_{ice}\Phi)/\partial y$], and (g),(h) the thermodynamic source/sink (Γ_Φ).

the larger tendency in the sea ice volume is applied to almost all latitudes, which suggests that the seasonality of the sea ice volume is the largest in $+v$, consistent with Fig. 4b. During the growth season, there is substantial additional freezing in the $+v$ run to the south of 65°S (Fig. 5h). This additional sea ice production increases the salt flux into the ocean, strengthening deep convection and the lower cell (see section 5 for further details). Conversely, during the melt season, additional melting in the $+v$ run across most regions leads to a greater decrease in the sea ice volume (Fig. 5g) with minimal influence of dynamic redistribution (Fig. 5e). In particular, greater

melting at lower latitudes increases the freshwater flux, reducing the ocean salinity. The sea ice volume budget in $-v$ exhibits the opposite changes (Figs. 5c,e,g), suggesting that the northerly wind anomaly reduces the seasonality of the sea ice volume and lowers the salt and freshwater flux into the ocean at higher and lower latitudes, respectively.

b. Tracer distributions

A southerly wind anomaly in $+v$ over the sea ice area leads to substantial changes in temperature and salinity, not only near the sea ice region but also in the broader Southern Ocean
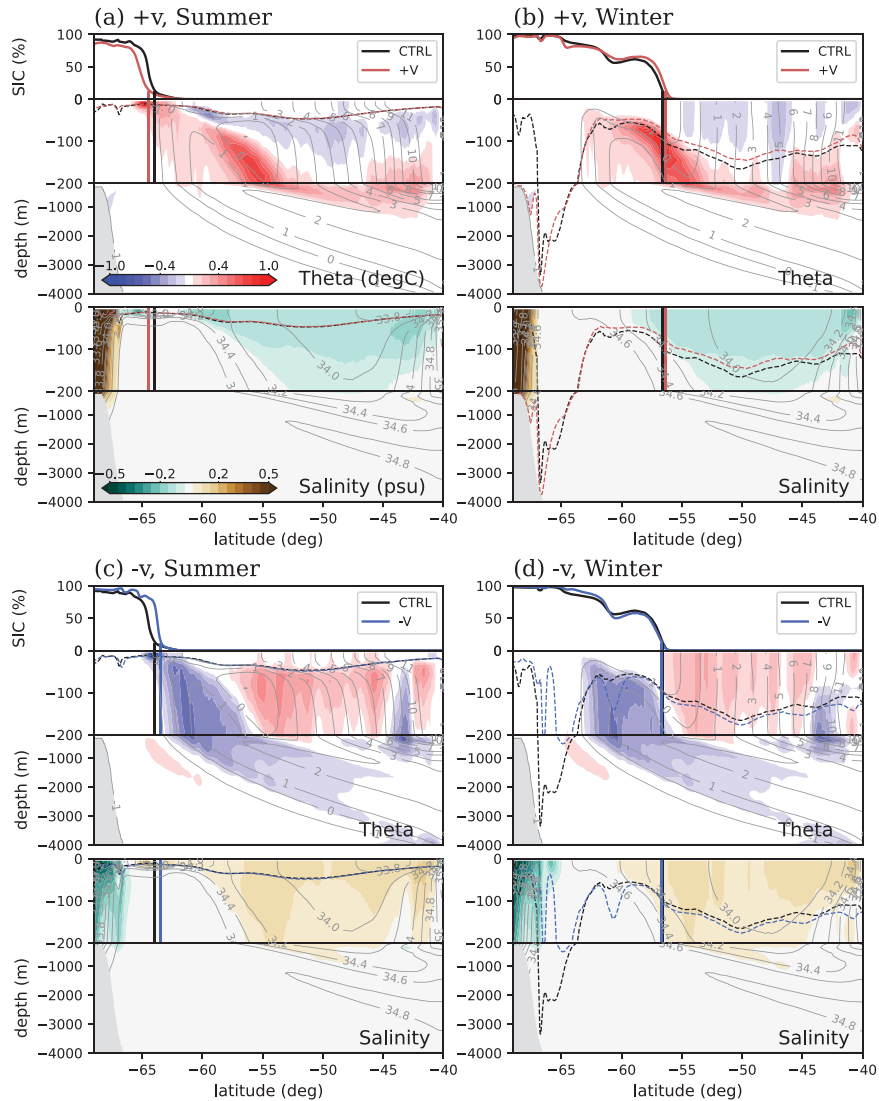
FIG. 6. Temperature and salinity differences between the perturbed and control simulations are shown for (a),(c) austral summer (January–March) and (b),(d) winter (July–September). Gray contour lines depict the mean fields from control simulations. Dashed lines indicate the mixed-layer depths in the control and perturbed simulations. The upper rectangle of each panel displays sea ice concentration as a function of latitude. Vertical lines represent the sea ice edges.

(Figs. 6a,b). In winter, a positive salinity anomaly appears near the coastal shelf, which can be attributed to the increased brine rejection from enhanced sea ice production within more widespread leads and polynyas. The increased mixed-layer depth reflects deeper convection from the enhanced sea ice production and salt flux into the ocean (Fig. 6b). In $+v$, the upper ocean north of the seasonal sea ice zone tends to be cooler and fresher than in CTRL, associated with the increased equatorward transport of cold and freshwater as inferred by the greater sea ice volume seasonality. At the subsurface, however, the temperature becomes up to 1°C warmer. The subsurface warming signal is attributed to the enhanced upwelling of warm subsurface water driven by

stronger upper and lower cells in $+v$. The surface warming at 65°S in summer is consistent with the surface expression of this warming and additional surface warming caused by sea ice loss leading to an increase in the absorption of incoming solar radiation. In summer, when the upper cell extends further south, this warming signal reaches the summer sea ice edge, leading to sea ice retreat to the south (Fig. 7c).

A northerly wind anomaly in $-v$ leads to responses which are generally opposite to those under the southerly wind anomaly: a decrease of salinity near the continental shelf, an increase of temperature and salinity to the north of the seasonal sea ice zone, and a negative anomaly of subsurface
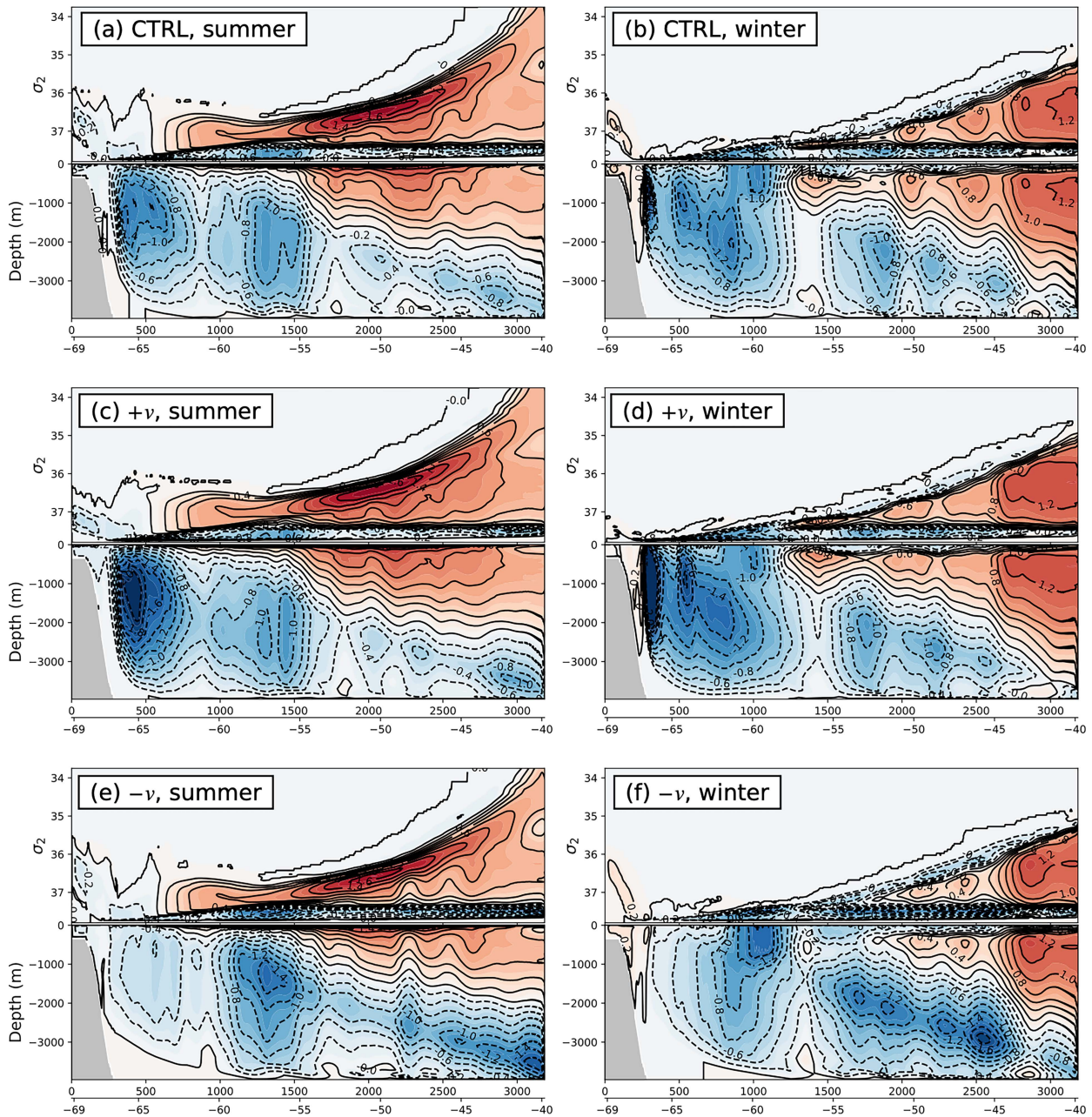
FIG. 7. Residual streamfunction Ψ in (top) σ_2 coordinate and (bottom) mapped on depth coordinate, averaged over austral (a),(c),(e) summer and (b),(d),(f) winter. The Ψ is shown for (a),(b) CTRL, (c),(d) $+v$, and (e),(f) $-v$ using both shading and contours in Sverdrups. The gray shading marks the topography.

temperature that reaches the surface near the sea ice edge in summer (Figs. 6c,d). The collocation of cooling and an increase in sea ice concentration at 65°S in the $-v$ simulation is consistent with enhanced ice coverage reducing the absorption of incoming solar radiation. The changes in surface conditions to the north of the seasonal sea ice zone are associated with a reduction in the equatorward transport of the cold and freshwater mass, which is suggested by the smaller sea ice seasonality in the $-v$ run. The northerly wind anomaly increases the

sea ice thickness, reduces the leads and polynyas, and suppresses the salt flux into the ocean and convection in winter, as suggested by the shallower mixed-layer depth (Fig. 6d). Then, the absence of deep convection near Antarctica leads to the weakening of the lower cell there, with its center shifted equatorward (Figs. 7e,f). These changes in the lower cell also shift the upwelling branch equatorward, leading to the subsurface cooling.

It is interesting to note that although the anomalies in the $+v$ and $-v$ runs are generally opposite in Fig. 6, they do not

necessarily have the same intensity or location. For example, the winter MLD anomaly between 65° and 67°S, where the MLD is deepest, is much larger in the $-v$ simulation, reaching several kilometers, while it is minor in the $+v$ simulation. With a larger winter MLD north of the sea ice edge in $-v$, the surface temperature anomaly penetrates deeper than in $+v$. Additionally, the subsurface temperature anomalies (positive in $+v$ and negative in $-v$) extend much deeper along the Circumpolar Deep Water in $-v$, while it is confined to the upper 1000 m in $+v$. These complex responses may result from the interaction between surface fluxes and ocean's internal processes, including vertical turbulent mixing and overturning circulation.

5. Changes in ocean circulation and their causal drivers

a. Overturning circulations

The channel model clearly captures the two overturning cells which are a prominent feature of the observed Southern Ocean: the upper cell transports the surface water equatorward and the lower cell transports surface waters poleward (red and blue shading in Fig. 7, respectively). In the control simulation (CTRL), the streamfunction in σ_2 coordinates shows transport along density surfaces, except in the upper ocean where surface buoyancy fluxes change the density of the water (upper part of Figs. 7a,b). The upper and lower cells separate near the location of zero zonal wind stress where water diverges due to the opposite direction of Ekman transport (not shown). The surface divergence is fed by an upwelling at the interface between the two cells. The vertical upwelling velocity w is given by $\partial\Psi/\partial y$, where Ψ is the meridional streamfunction. The upwelling velocity can be up to $O(0.1)$ m day^{-1}. Deep convection occurs near 67°S, especially in winter, and extends from the surface almost to the bottom of the domain (Figs. 7a,b). South of 67°S, the sea ice concentration is nearly 100% and there is rarely sea ice production in our channel model.

The southerly wind anomaly in $+v$ significantly impacts the residual overturning circulation, particularly the intensification of the bottom water formation in both austral summer and winter (Figs. 7c,d). While the upper cell shows a slight increase in intensity, the intensification of the lower cell is the dominant response to the southerly wind anomaly. This is evident in the annual mean Ψ, which has a maximum strength of -2.1 Sv (1 Sv $\equiv 10^6$ m^3 s^{-1}), 50% stronger than that in CTRL. This intensification is driven by brine rejection where the sea ice concentration falls below 1 near 67°S (Fig. 4e). The strength of the upwelling branch between the upper and lower cells depends on the gradient of Ψ across the contours. Therefore, the intensification of the lower cell and the tighter contour spacing in Ψ lead to a stronger transport of warm subsurface water upward toward the sea ice and potentially affect the sea ice.

In contrast, the northerly wind anomaly in $-v$ weakens the lower cell near Antarctica in both austral summer and winter (Figs. 7e,f). The annually averaged maximum strength of Ψ to the south of 60°S is less than -0.7 Sv, which is 50% weaker than that in CTRL. Notably, the prominent wintertime convection observed in both CTRL and $+v$ is absent in $-v$, which is related to the lower salt flux and heat loss in the region to the south of 65°S (Fig. 4c). Another change in the lower cell is the equatorward shift of its center, resulting in the upwelling branch shifting equatorward compared to other simulations. The upper cell is also weaker under the northerly wind anomaly. These changes of the overturning cells lead to the subsurface cooling along the upwelling branch seen in CTRL.

Before going on, we should note an important caveat. The lower cell in our channel model does not connect directly to the shelf region, suggesting that it is primarily maintained and fed through open ocean convection. This is in contrast from inferences made from observations (Silvano et al. 2023). Our model, like many others, and in particular global climate model, de-emphasizes shelf processes.

b. Water-mass transformation rate

1) CONTRIBUTION FROM SURFACE HEAT FLUX

The surface heat flux leads to a positive water-mass transformation rate (increasing density) in fall and winter but a negative rate (decreasing density) in spring and summer (Figs. 8c,f,i,l). During fall and winter, when the air temperature is colder than the surface ocean temperature, there is an oceanic heat loss that leads to an increase in surface density. This densification is particularly evident in winter in the seasonal sea ice zone ($37.5 > \sigma_2 > 37.0$ kg m^{-3}) and in the water mass with $\sigma_2 > 37.5$ kg m^{-3} located in the region to the south of 65°S, which suggests that there is considerable heat loss whenever there is an opening in the sea ice in fall and winter. By definition, the volume flux associated with a positive water-mass transformation rate is toward higher density class, which implies that the surface heat flux contributes to the poleward transport of the surface water in fall and winter. In fact, the lower cell extends equatorward during this season, supporting the surface poleward transport (Figs. 7b,d,f). As the season progresses, the ocean takes up the heat from the atmosphere, and the surface density decreases until the fall when the ocean starts to lose heat to the atmosphere again, which means that the heat flux acts to drive the equatorward transport of the surface water and feeds the upper cell. This is further supported by the poleward extension of the upper cell that has an equatorward transport near the surface during spring and summer (Figs. 7a,c,e).

The southerly wind anomaly, $+v$, slightly reduces the positive water-mass transformation rate by the surface heat flux in winter but amplifies the negative rate in summer (red lines in Figs. 8a,g). These changes are related to the sea ice extent. In $+v$, the larger sea ice extent in winter (Fig. 4a) limits the air–sea heat exchange more than in the control run, resulting in reduced heat loss. Leads and polynyas in Fig. 4e occur in the water mass of $\sigma_2 \sim 37.7$ kg m^{-3} and serve as a site of heat loss and densification, as marked by the peak in the water-mass transformation rate in winter (Fig. 8a). In summer, however, $+v$ has a smaller sea ice extent than the control run, allowing more heat uptake and a greater negative transformation rate.

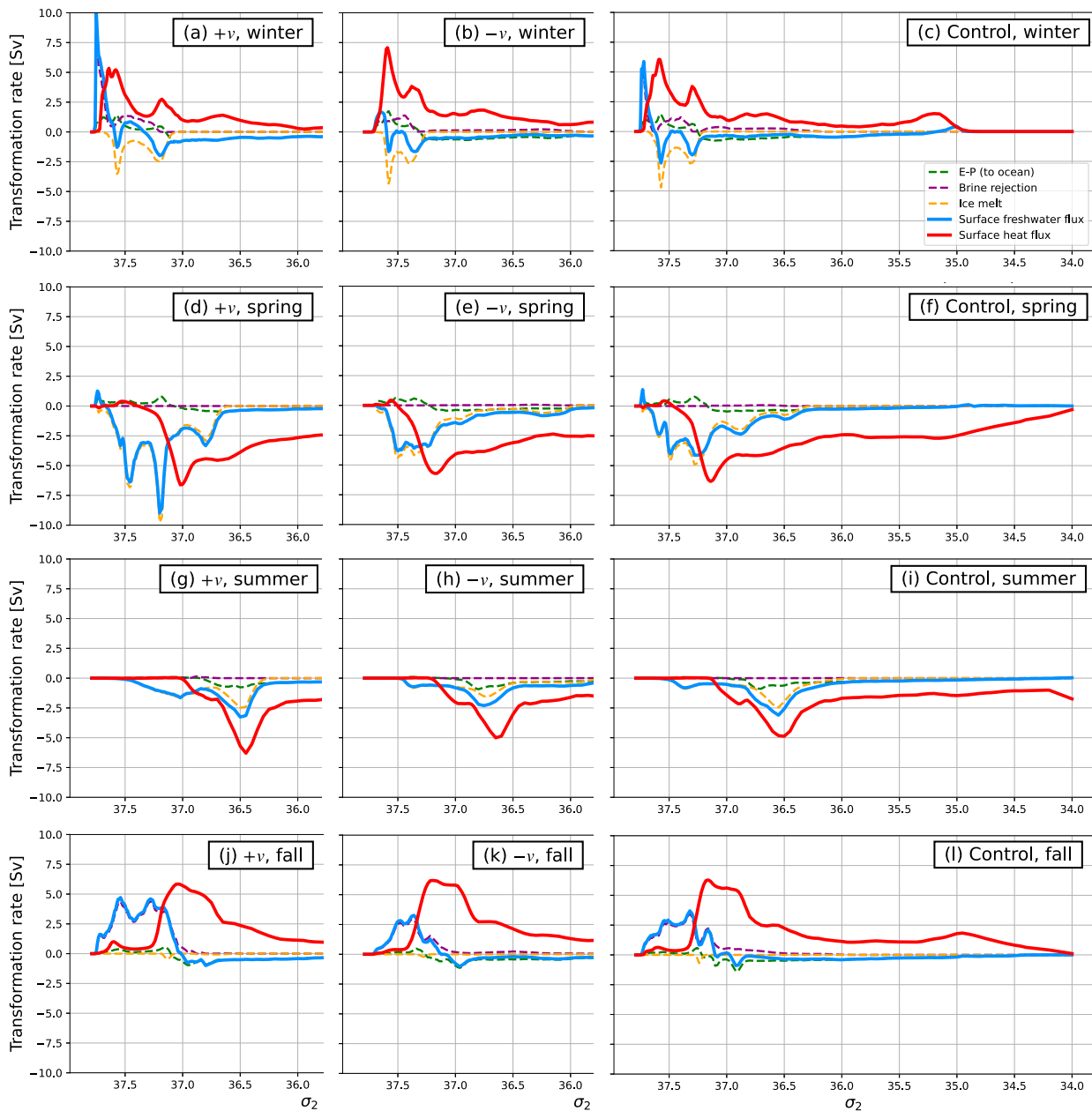## Water-mass transformation rate (Sv)

FIG. 8. The water-mass transformation rate by surface heat flux (solid red) and freshwater flux (solid blue) in (a),(d),(g),(j) $+v$, (b),(e),(h),(k) $-v$, and (c),(f),(i),(l) control run as a function of σ_2 (kg m^{-3}) for austral (a)–(c) winter (July–September), (d)–(f) spring (October–December), (g)–(i) summer (January–March), and (j)–(k) fall (April–June). Positive values indicate an increase in the density of the seawater. The transformation rate by freshwater flux is partitioned into the difference between evaporation and precipitation (dashed green) and ocean–ice interaction that is the sum of brine rejection (dashed purple) and sea ice melting (dashed orange). It is noted that the x axis ranges differ between the experiments.

The northerly wind anomaly leads to a marginal increase in the positive transformation rate in winter when compared with CTRL (Fig. 8b). This increase occurs in the water mass of $\sigma_2 \sim 37.6$ kg m^{-3} that can be found near 61°S in winter

where the sea ice concentration in $-v$ is lower than CTRL. In summer, the size of the negative water-mass transformation rate by the heat flux in $-v$ is comparable with CTRL, but there is a shift of the negative peak toward higher density class

in $-v$ (Fig. 8h), which is associated with the higher density of the surface water. The lower sea ice seasonal variability in $-v$ results in the reduced equatorward freshwater transport, leading to a higher surface density than the other simulations.

2) CONTRIBUTION FROM SURFACE FRESHWATER FLUX

The freshwater flux can be partitioned into two components in this channel model: freshwater flux between atmosphere and ocean and between sea ice and ocean. The freshwater flux between atmosphere and ocean results from the difference between evaporation and precipitation, while sea ice formation and melting determine the freshwater flux between sea ice and ocean. The size of the water-mass transformation rate by freshwater flux is generally smaller than that by heat flux in the control simulation, except where sea ice formation and melting occur (Figs. 8c,f,i,l). In winter, the sea ice production has a positive transformation rate in the highest density class, showing that it is directly involved with bottom water formation (dashed purple line in Fig. 8c). The water mass that becomes the bottom water is cooled by surface heat fluxes at $\alpha_2 \approx 37.6$ kg m^{-3}. The final increase in density is supplied through brine rejection from sea ice formation. In spring and summer, the freshening of the surface water by sea ice melting occurs in a lower density class than that of sea ice formation, indicating that there is a net freshwater transport from dense water masses to lighter water masses (dashed orange lines in Figs. 8f,i). The transformation rate by the freshwater flux between the atmosphere and the ocean shows a negligible contribution in the region south of the seasonal sea ice zone with 37.2 kg m$^{-3} > \sigma_2$ (dashed green lines in Figs. 8c,f,i,l), which can be explained by the presence of the sea ice that blocks the freshwater flux between them.

The southerly wind anomaly amplifies the water-mass transformation rate by freshwater flux (Figs. 8a,d,g,j). In particular, the sea ice formation and melting contribute to this amplification, showing nearly 10 Sv in winter and -10 Sv in spring, respectively. The increased positive transformation rate in winter is consistent with the intensification of the deep convection and the lower cell in $+v$ (Figs. 7c,d). In spring, the enhanced negative transformation rate in the seasonal sea ice zone shows the largest freshwater flux into the ocean by the sea ice melting among the three simulations, which is in agreement with the lowest sea ice extent in $+v$ (Fig. 4a). This freshwater flux into the ocean leads to a lower surface salinity (Figs. 6a,b). Considering the transformation rates by both heat and freshwater fluxes, the volume transport toward lower density class in spring is the greatest in $+v$, leading to a slight increase of the upper cell.

In contrast, the deep convection weakens in $-v$, and the sea ice formation and melting tend to occur only in the seasonal sea ice zone (Figs. 8b,e,h,k). The densification of the surface water occurs mainly through heat loss within a relatively light water mass compared to the other simulations (Fig. 8b). As a result, the core of the lower cell moves farther north, which shifts the upwelling branch equatorward (Figs. 7e,f). The upper cell also slightly loses strength, which is in agreement with the reduced negative transformation rate in the seasonal sea

ice zone and increased surface salinity (Figs. 6c,d). The reduced intensity of the formation rate by brine rejection and sea ice melting is consistent with a smaller seasonal cycle of sea ice, which is indeed observed in $-v$ (Figs. 4a,b).

6. Conclusions and discussion

The surface wind near Antarctic sea ice plays a critical role in sea ice and oceanic processes that lead to bottom water formation and control the lower cell of the meridional overturning circulation. In this study, we aim to answer the question of how the strength of the meridional wind influences sea ice distribution and ocean circulation in the Southern Ocean using observations and an idealized eddy-resolving coupled ocean–sea ice model. The idealized configuration of the model allows us to eliminate complications due to zonal asymmetry and interannual variability while successfully reproducing not only the mean states of the sea ice and oceanic variables but also the two meridional overturning cells.

The sea ice, ocean states, and meridional circulation show distinct responses depending on the sign of the perturbation in the meridional wind in the sea ice zone. The southerly wind perturbation increases the seasonal variation in the sea ice extent: with broader sea ice extent in austral winter but smaller in austral summer compared with the control simulation. The seasonal variation in the sea ice volume also becomes greater than the control simulation, indicating the enhancement of sea ice production and the equatorward freshwater transport. There is a substantial increase in leads and polynyas under the southerly wind perturbation in winter, where there is an oceanic heat loss and salt flux into the ocean due to sea ice formation. The water-mass transformation rate analysis reveals that these changes in the surface buoyancy flux result in volume fluxes toward higher density classes, eventually forming bottom water. The enhancement of bottom water formation strengthens the lower cell of the residual meridional overturning circulation and increases the rate at which relatively warm water is upwelled toward the summertime sea ice edge, promoting more sea ice melt there.

The northerly wind perturbation leads to the opposite response in the sea ice and ocean circulation. The seasonal variation of the sea ice extent is reduced with summertime extent increased and wintertime extent decreased. The sea ice volume, however, is larger in the $-v$ simulation than the other two simulations in all seasons, suggesting that the thickness of the sea ice is the greatest with the northerly meridional wind perturbation. This is especially true in winter when sea ice extent is the smallest, but volume is largest. The larger volume of sea ice in higher latitudes (south of 65°S) suppresses the surface buoyancy flux and the formation of bottom water, as shown by the water-mass transformation analysis. As a result, the lower cell has its core and upwelling branch shifted further north than in the other two simulations, yielding relatively cooler water along the upwelling branch of the control simulation. These changes contribute to greater sea ice extent and volume in the summer.

The simplicity of this study may not fully explain the observed and anticipated changes to sea ice and ocean circulation,

especially if the wind forcing has zonally asymmetric components. The bottom topography, a fundamental component in the momentum balance, is flat in our experiment. In addition, the time-invariant wind perturbations are not consistent with the seasonal differences in the observed meridional wind trend (Hazel and Stewart 2019). It should also be noted that an important aspect is missing—viz the diminished role of shelf processes in water-mass transformation relative to the observations. These shortcomings will be addressed in future studies where the meridional wind perturbations force a global ocean–sea ice model.

The results from this idealized model clearly show that meridional wind perturbations near the Antarctic sea ice region can have substantial and widespread impacts on the sea ice and ocean circulation. A series of well-coordinated processes between the sea ice and buoyancy-driven ocean circulation deliver the impact of surface wind perturbations down to the bottom of the Southern Ocean, emphasizing the importance of better representing the meridional winds for a more accurate simulation of the sea ice and the Southern Ocean. This is particularly important given that there is a relatively large spread in the surface wind among the existing reanalysis products (Dong et al. 2020). Hence, the results from this study may provide insights on what to anticipate in sea ice and Southern Ocean simulations when a particular reanalysis product is chosen to force the model.

Future projections of meridional wind near the Antarctic sea ice indicate we should anticipate wind-driven changes to the sea ice and oceanic states in the Southern Ocean. CMIP6 models project an overall weakening of the southerly wind by 2% and 7% at the end of the century under the intermediate and very high greenhouse gas emission scenarios [Shared Socioeconomic Pathway (SSP2-4.5 and SSP5-8.5)], respectively, with local changes in meridional wind ranging from approximately -0.5 and 0.5 m s^{-1} (Neme et al. 2022). It is plausible that these meridional wind perturbations could result in a significant change in the strength of the lower cell locally. If these meridional wind changes align with dense shelf water formation regions, then we are likely to see significant changes to the formation of bottom water. Hence, the meridional wind needs to be taken into consideration in the future projection of Antarctic sea ice.

Data availability statement. The satellite sea–ice concentration data used in the study are available at NASA National Snow and Ice Data Center (https://nsidc.org/data/NSIDC-0051/versions/2). The ERA5 reanalysis data for 10-m winds can be accessed from the Copernicus Climate Data Store (https://cds.climate.copernicus.eu/cdsapp#!/dataset/reanalysis-era5-single-levels-monthly-means?tab=form). Both datasets are freely available with citations DiGirolamo et al. (2022) and Hersbach et al. (2023), respectively. The MITgcm can be obtained from http://mitgcm.org website. The model's configuration is available at https://doi.org/10.5281/zenodo.11195066 and output is available upon request.

REFERENCES

Abernathey, R. P., I. Cerovecki, P. R. Holland, E. Newsom, M. Mazloff, and L. D. Talley, 2016: Water-mass transformation by sea ice in the upper branch of the Southern Ocean overturning. *Nat. Geosci.*, **9**, 596–601, https://doi.org/10.1038/ngeo2749.

Adcroft, A., C. Hill, and J. Marshall, 1997: Representation of topography by shaved cells in a height coordinate ocean model. *Mon. Wea. Rev.*, **125**, 2293–2315, https://doi.org/10.1175/1520-0493(1997)125<2293:ROTBSC>2.0.CO;2.

——, ——, J.-M. Campin, J. Marshall, and P. Heimbach, 2004: Overview of the formulation and numerics of the MIT GCM. *Proc. ECMWF Seminar Series on Numerical Methods, Recent Developments in Numerical Methods for Atmosphere and Ocean Modelling*, Reading, United Kingdom, ECMWF, 139–149, https://www.ecmwf.int/sites/default/files/elibrary/2004/7642-overview-formulation-and-numerics-mit-gcm.pdf.

Al-Shehhi, M. R., H. Song, J. Scott, and J. Marshall, 2021: Water mass transformation and overturning circulation in the Arabian Gulf. *J. Phys. Oceanogr.*, **51**, 3513–3527, https://doi.org/10.1175/JPO-D-20-0249.1.

Armour, K. C., J. Marshall, J. R. Scott, A. Donohoe, and E. R. Newsom, 2016: Southern Ocean warming delayed by circumpolar upwelling and equatorward transport. *Nat. Geosci.*, **9**, 549–554, https://doi.org/10.1038/ngeo2731.

Bader, J., M. Flügge, N. G. Kvamstø, M. D. S. Mesquita, and A. Voigt, 2013: Atmospheric winter response to a projected future Antarctic sea-ice reduction: A dynamical analysis. *Climate Dyn.*, **40**, 2707–2718, https://doi.org/10.1007/s00382-012-1507-9.

Barthélemy, A., H. Goosse, P. Mathiot, and T. Fichefet, 2012: Inclusion of a katabatic wind correction in a coarse-resolution global coupled climate model. *Ocean Modell.*, **48**, 45–54, https://doi.org/10.1016/j.ocemod.2012.03.002.

Bintanja, R., G. J. van Oldenborgh, S. Drijfhout, B. Wouters, and C. A. Katsman, 2013: Important role for ocean warming and increased ice-shelf melt in Antarctic sea-ice expansion. *Nat. Geosci.*, **6**, 376–379, https://doi.org/10.1038/ngeo1767.

Campbell, E. C., E. A. Wilson, G. W. K. Moore, S. C. Riser, C. E. Brayton, M. R. Mazloff, and L. D. Talley, 2019: Antarctic offshore polynyas linked to Southern Hemisphere climate anomalies. *Nature*, **570**, 319–325, https://doi.org/10.1038/s41586-019-1294-0.

Cavalieri, D. J., and C. L. Parkinson, 2008: Antarctic sea ice variability and trends, 1979–2006. *J. Geophys. Res.*, **113**, C07004, https://doi.org/10.1029/2007JC004564.

Chelton, D. B., R. A. deSzoeke, M. G. Schlax, K. E. Naggar, and N. Siwertz, 1998: Geographical variability of the first baroclinic Rossby radius of deformation. *J. Phys. Oceanogr.*, **28**, 433–460, https://doi.org/10.1175/1520-0485(1998)028%3C0433:GVOTFB%3E2.0.CO;2.

Comiso, J. C., and F. Nishio, 2008: Trends in the sea ice cover using enhanced and compatible AMSR-E, SSM/I, and SMMR data. *J. Geophys. Res.*, **113**, C02S07, https://doi.org/10.1029/2007JC004257.

——, R. A. Gersten, L. V. Stock, J. Turner, G. J. Perez, and K. Cho, 2017: Positive trend in the Antarctic sea ice cover and associated changes in surface temperature. *J. Climate*, **30**, 2251–2267, https://doi.org/10.1175/JCLI-D-16-0408.1.

Dale, E. R., A. J. McDonald, J. H. Coggins, and W. Rack, 2017: Atmospheric forcing of sea ice anomalies in the Ross Sea polynya region. *Cryosphere*, **11**, 267–280, https://doi.org/10.5194/tc-11-267-2017.

DiGirolamo, N., C. L. Parkinson, D. J. Cavalieri, P. Gloersen, and H. J. Zwally, 2022: Sea ice concentrations from Nimbus-7 SMMR and DMSP SSM/I-SSMIS Passive Microwave Data, version 2. NASA National Snow and Ice Data Center Distributed Active Archive Center, accessed 28 September 2024, https://doi.org/10.5067/MPYG15WAA4WX.

Doddridge, E. W., J. Marshall, H. Song, J.-M. Campin, and M. Kelley, 2021: Southern Ocean heat storage, reemergence, and winter sea ice decline induced by summertime winds. *J. Climate*, **34**, 1403–1415, https://doi.org/10.1175/JCLI-D-20-0322.1.

Dong, X., Y. Wang, S. Hou, M. Ding, B. Yin, and Y. Zhang, 2020: Robustness of the recent global atmospheric reanalyses for Antarctic near-surface wind speed climatology. *J. Climate*, **33**, 4027–4043, https://doi.org/10.1175/JCLI-D-19-0648.1.

Ferrari, R., M. F. Jansen, J. F. Adkins, A. Burke, A. L. Stewart, and A. F. Thompson, 2014: Antarctic sea ice control on ocean circulation in present and glacial climates. *Proc. Natl. Acad. Sci. USA*, **111**, 8753–8758, https://doi.org/10.1073/pnas.1323922111.

Ferreira, D., J. Marshall, C. M. Bitz, S. Solomon, and A. Plumb, 2015: Antarctic Ocean and sea ice response to ozone depletion: A two-time-scale problem. *J. Climate*, **28**, 1206–1226, https://doi.org/10.1175/JCLI-D-14-00313.1.

Gaspar, P., Y. Grégoris, and J.-M. Lefevre, 1990: A simple eddy kinetic energy model for simulations of the oceanic vertical mixing: Tests at station Papa and long-term upper ocean study site. *J. Geophys. Res.*, **95**, 16 179–16 193, https://doi.org/10.1029/JC095iC09p16179.

Haumann, F. A., D. Notz, and H. Schmidt, 2014: Anthropogenic influence on recent circulation-driven Antarctic sea ice changes. *Geophys. Res. Lett.*, **41**, 8429–8437, https://doi.org/10.1002/2014GL061659.

——, N. Gruber, M. Münnich, I. Frenger, and S. Kern, 2016: Sea-ice transport driving Southern Ocean salinity and its recent trends. *Nature*, **537**, 89–92, https://doi.org/10.1038/nature19101.

Hazel, J. E., and A. L. Stewart, 2019: Are the near-Antarctic easterly winds weakening in response to enhancement of the southern annular mode? *J. Climate*, **32**, 1895–1918, https://doi.org/10.1175/JCLI-D-18-0402.1.

Hersbach, H., and Coauthors, 2023: ERA5 monthly averaged data on single levels from 1940 to present. Copernicus Climate Change Service (C3S) Climate Data Store (CDS), accessed 10 March 2021, https://doi.org/10.24381/cds.f17050d7.

Holland, P. R., and R. Kwok, 2012: Wind-driven trends in Antarctic sea-ice drift. *Nat. Geosci.*, **5**, 872–875, https://doi.org/10.1038/ngeo1627.

Kidston, J., A. S. Taschetto, D. W. J. Thompson, and M. H. England, 2011: The influence of Southern Hemisphere sea-ice extent on the latitude of the mid-latitude jet stream. *Geophys. Res. Lett.*, **38**, L15804, https://doi.org/10.1029/2011GL048056.

Kim, S.-J., and A. Stössel, 1998: On the representation of the Southern Ocean water masses in an ocean climate model. *J. Geophys. Res.*, **103**, 24 891–24 906, https://doi.org/10.1029/98JC02413.

Kwok, R., S. S. Pang, and S. Kacimi, 2017: Sea ice drift in the Southern Ocean: Regional patterns, variability, and trends. *Elementa Sci. Anthrop.*, **5**, 32, https://doi.org/10.1525/elementa.226.

Large, W. G., and S. Pond, 1982: Sensible and latent head flux measurements over the ocean. *J. Phys. Oceanogr.*, **12**, 464–482, https://doi.org/10.1175/1520-0485(1982)012%3C0464:SALHFM%3E2.0.CO;2.

——, and S. G. Yeager, 2009: The global climatology of an interannually varying air–sea flux data set. *Climate Dyn.*, **33**, 341–364, https://doi.org/10.1007/s00382-008-0441-3.

Libera, S., W. Hobbs, A. Klocker, A. Meyer, and R. Matear, 2022: Ocean-sea ice processes and their role in multi-month predictability of Antarctic sea ice. *Geophys. Res. Lett.*, **49**, e2021GL097047, https://doi.org/10.1029/2021GL097047.

Locarnini, R. A., and Coauthors, 2013: Temperature. *World Ocean Atlas 2013*, NOAA Atlas NESDIS 73, 40 pp.

Marshall, J., and K. Speer, 2012: Closure of the meridional overturning circulation through Southern Ocean upwelling. *Nat. Geosci.*, **5**, 171–180, https://doi.org/10.1038/ngeo1391.

——, A. Adcroft, C. Hill, L. Perelman, and C. Heisey, 1997a: A finite-volume, incompressible Navier Stokes model for studies of the ocean on parallel computers. *J. Geophys. Res.*, **102**, 5753–5766, https://doi.org/10.1029/96JC02775.

——, C. Hill, L. Perelman, and A. Adcroft, 1997b: Hydrostatic, quasi-hydrostatic, and nonhydrostatic ocean modeling. *J. Geophys. Res.*, **102**, 5733–5752, https://doi.org/10.1029/96JC02776.

——, H. Jones, and C. Hill, 1998: Efficient ocean modeling using non-hydrostatic algorithms. *J. Mar. Syst.*, **18**, 115–134, https://doi.org/10.1016/S0924-7963(98)00008-6.

——, D. Jamous, and J. Nilsson, 1999: Reconciling thermodynamic and dynamic methods of computation of water-mass transformation rates. *Deep-Sea Res. I*, **46**, 545–572, https://doi.org/10.1016/S0967-0637(98)00082-X.

Morales Maqueda, M. A., A. J. Willmott, and N. R. T. Biggs, 2004: Polynya dynamics: A review of observations and modeling. *Rev. Geophys.*, **42**, RG1004, https://doi.org/10.1029/2002RG000116.

Neme, J., M. H. England, and A. M. Hogg, 2022: Projected changes of surface winds over the Antarctic continental margin. *Geophys. Res. Lett.*, **49**, e2022GL098820, https://doi.org/10.1029/2022GL098820.

Nishikawa, S., H. Tsujino, K. Sakamoto, and H. Nakano, 2013: Diagnosis of water mass transformation and formation rates in a high-resolution GCM of the North Pacific. *J. Geophys. Res. Oceans*, **118**, 1051–1069, https://doi.org/10.1029/2012JC008116.

OSI SAF, 2022: Global sea ice concentration climate data record v3. 0-multimission. EUMETSAT SAF on Ocean and Sea Ice, accessed 5 November 2024, https://doi.org/10.15770/EUM_SAF_OSI_0013.

Parish, T. R., and K. T. Waight III, 1987: The forcing of Antarctic katabatic winds. *Mon. Wea. Rev.*, **115**, 2214–2226, https://doi.org/10.1175/1520-0493(1987)115%3C2214:TFOAKW%3E2.0.CO;2.

Parkinson, C. L., and D. J. Cavalieri, 2012: Antarctic sea ice variability and trends, 1979–2010. *Cryosphere*, **6**, 871–880, https://doi.org/10.5194/tc-6-871-2012.

Pavelsky, T. M., J. Boé, A. Hall, and E. J. Fetzer, 2011: Atmospheric inversion strength over polar oceans in winter

regulated by sea ice. *Climate Dyn.*, **36**, 945–955, https://doi.org/10.1007/s00382-010-0756-8.

Pauling, A. G., C. M. Bitz, I. J. Smith, and P. J. Langhorne, 2016: The response of the Southern Ocean and Antarctic sea ice to freshwater from ice shelves in an earth system model. *J. Climate*, **29**, 1655–1672, https://doi.org/10.1175/JCLI-D-15-0501.1.

Pease, C. H., 1987: The size of wind-driven coastal polynyas. *J. Geophys. Res.*, **92**, 7049–7059, https://doi.org/10.1029/JC092iC07p07049.

Pinardi, N., P. Cessi, F. Borile, and C. L. P. Wolfe, 2019: The Mediterranean Sea overturning circulation. *J. Phys. Oceanogr.*, **49**, 1699–1721, https://doi.org/10.1175/JPO-D-18-0254.1.

Purich, A., and E. W. Doddridge, 2023: Record low Antarctic sea ice coverage indicates a new sea ice state. *Commun. Earth Environ.*, **4**, 314, https://doi.org/10.1038/s43247-023-00961-9.

——, and M. H. England, 2023: Projected impacts of Antarctic meltwater anomalies over the twenty-first century. *J. Climate*, **36**, 2703–2719, https://doi.org/10.1175/JCLI-D-22-0457.1.

——, W. Cai, M. H. England, and T. Cowan, 2016: Evidence for link between modelled trends in Antarctic sea ice and underestimated westerly wind changes. *Nat. Commun.*, **7**, 10409, https://doi.org/10.1038/ncomms10409.

Rye, C. D., J. Marshall, M. Kelley, G. Russell, L. S. Nazarenko, Y. Kostov, G. A. Schmidt, and J. Hansen, 2020: Antarctic glacial melt as a driver of recent Southern Ocean climate trends. *Geophys. Res. Lett.*, **47**, e2019GL086892, https://doi.org/10.1029/2019GL086892.

Schroeter, S., and P. A. Sandery, 2022: Large-ensemble analysis of Antarctic sea ice model sensitivity to parameter uncertainty. *Ocean Modell.*, **177**, 102090, https://doi.org/10.1016/j.ocemod.2022.102090.

Silvano, A., and Coauthors, 2023: Observing Antarctic Bottom Water in the Southern Ocean. *Front. Mar. Sci.*, **10**, 1221701, https://doi.org/10.3389/fmars.2023.1221701.

Simmonds, I., and M. Li, 2021: Trends and variability in polar sea ice, global atmospheric circulations, and baroclinicity. *Ann. N. Y. Acad. Sci.*, **1504**, 167–186, https://doi.org/10.1111/nyas.14673.

Smith, S. D., R. D. Muench, and C. H. Pease, 1990: Polynyas and leads: An overview of physical processes and environment. *J. Geophys. Res.*, **95**, 9461–9479, https://doi.org/10.1029/JC095iC06p09461.

Smith, D. M., N. J. Dunstone, A. A. Scaife, E. K. Fiedler, D. Copsey, and S. C. Hardiman, 2017: Atmospheric response to Arctic and Antarctic sea ice: The importance of ocean–atmosphere coupling and the background state. *J. Climate*, **30**, 4547–4565, https://doi.org/10.1175/JCLI-D-16-0564.1.

Stammerjohn, S. E., M. R. Drinkwater, R. C. Smith, and X. Liu, 2003: Ice-atmosphere interactions during sea-ice advance and retreat in the western Antarctic Peninsula region. *J. Geophys. Res.*, **108**, 3329, https://doi.org/10.1029/2002JC001543.

Stein, K., A. Timmermann, E. Y. Kwon, and T. Friedrich, 2020: Timing and magnitude of Southern Ocean sea ice/carbon cycle feedbacks. *Proc. Natl. Acad. Sci. USA*, **117**, 4498–4504, https://doi.org/10.1073/pnas.1908670117.

Tamura, T., K. I. Ohshima, and S. Nihashi, 2008: Mapping of sea ice production for Antarctic coastal polynyas. *Geophys. Res. Lett.*, **35**, L07606, https://doi.org/10.1029/2007GL032903.

Thompson, D. W. J., and S. Solomon, 2002: Interpretation of recent Southern Hemisphere climate change. *Science*, **296**, 895–899, https://doi.org/10.1126/science.1069270.

Turner, J., and Coauthors, 2009: Non-annular atmospheric circulation change induced by stratospheric ozone depletion and its role in the recent increase of Antarctic sea ice extent. *Geophys. Res. Lett.*, **36**, L08502, https://doi.org/10.1029/2009GL037524.

——, J. S. Hosking, G. J. Marshall, T. Phillips, and T. J. Bracegirdle, 2016: Antarctic sea ice increase consistent with intrinsic variability of the Amundsen Sea Low. *Climate Dyn.*, **46**, 2391–2402, https://doi.org/10.1007/s00382-015-2708-9.

Walin, G., 1982: On the relation between sea-surface heat flow and thermal circulation in the ocean. *Tellus*, **34A**, 187–195, https://doi.org/10.3402/tellusa.v34i2.10801.

Wall, C. J., T. Kohyama, and D. L. Hartmann, 2017: Low-cloud, boundary layer, and sea ice interactions over the Southern Ocean during winter. *J. Climate*, **30**, 4857–4871, https://doi.org/10.1175/JCLI-D-16-0483.1.

Wagner, T. J. W., I. Eisenman, and H. C. Mason, 2021: How sea ice drift influences sea ice area and volume. *Geophys. Res. Lett.*, **48**, e2021GL093069, https://doi.org/10.1029/2021GL093069.

Zweng, M., and Coauthors, 2013: Salinity. *World Ocean Atlas 2013*, NOAA Atlas NESDIS 74, 39 pp.